Chemical Science

ROYAL SOCIETY OF CHEMISTRY

EDGE ARTICLE

View Article Online
View Journal | View Issue

Cite this: *Chem. Sci.*, 2023, **14**, 12774

All publication charges for this article have been paid for by the Royal Society of Chemistry

A $Cu^{I}Co^{II}$ cryptate for the visible light-driven reduction of CO_2†

Julia Jökel,[a] Esma Birsen Boydas,[b] Joël Wellauer,[c] Oliver S. Wenger,[c] Marc Robert,[de] Michael Römelt *[b] and Ulf-Peter Apfel *[af]

Received 26th May 2023
Accepted 25th October 2023

DOI: 10.1039/d3sc02679e

rsc.li/chemical-science

Among the rare bimetallic complexes known for the reduction of CO_2, $Co^{II}Co^{II}$ and $Zn^{II}Co^{II}$ hexamine cryptates are described as efficient photocatalysts. In close relation to the active sites of natural, CO_2-reducing enzymes, we recently reported the asymmetric cryptand $\{N^SN^N\}_m$ ($\{N^SN^N\}_m$ = N[$(CH_2)_2SCH_2(m\text{-}C_6H_4)CH_2NH(CH_2)_2]_3$N) comprising distinct sulphur- and nitrogen-rich binding sites and the corresponding $Cu^{I}M^{II}$ (M^{II} = Co^{II}, Ni^{II}, Cu^{II}) complexes. To gain insight into the effect of metals in different oxidation states and sulphur-incorporation on the photocatalytic activity, we herein investigate the $Cu^{I}Co^{II}$ complex of $\{N^SN^N\}_m$ as catalyst for the visible light-driven reduction of CO_2. After 24 h irradiation with LED light of 450 nm, $Cu^{I}Co^{II}$-$\{N^SN^N\}_m$ shows a high efficiency for the photocatalytic CO_2-to-CO conversion with 9.22 μmol corresponding to a turnover number of 2305 and a high selectivity of 98% over the competing H_2 production despite working in an acetonitrile/water (4 : 1) mixture. Experiments with mononuclear counterparts and computational studies show that the high activity can be attributed to synergistic catalysis between Cu and Co. Furthermore, it was shown that an increase of the metal distance results in the loss of synergistic effects and rather single-sited Co catalysis is observed.

Introduction

Artificial photosynthesis is a promising alternative to meet the increasing energy demand which has been, until now, mainly covered by the combustion of fossil fuels.[1–3] With the use of abundant resources like sunlight and water, the reduction of CO_2 into renewable fuels like CO, CH_4, formic acid or methanol, is a viable approach for completing the carbon cycle.[4,5] Although tremendous efforts have been devoted to the development of heterogeneous catalysts for the photocatalytic CO_2 reduction, low yields together with a missing profound insight into reaction mechanisms make an industrial application not yet feasible.[6–8]

To get a fundamental understanding of important structural features or mechanistic details of an efficient photocatalytic CO_2 reduction, homogeneous catalysis is a helpful tool.[9] Moreover, the manifold spectroscopic techniques available for homogeneous catalysis allow for a specific fine-tuning of the catalyst's structure on a molecular level.[9–12]

Typically, homogeneous photocatalytic systems comprise three components: a photosensitiser for harvesting and converting light into electrochemical potential, a sacrificial reductant providing the required electrons and a molecular catalyst for accumulating and transferring them to the substrate.[13,14] Due to the cruciality of the last step, many studies focus on the design of molecular catalysts.[11,15–17]

In contrast to the required harsh conditions and low selectivity associated with the artificial reduction of CO_2, the naturally occurring enzymes CO dehydrogenases (CODHs) can convert CO_2 selectively into CO under mild conditions.[18] They commonly have heterobimetallic active sites comprised of frustrated Lewis pairs (*e.g.* Ni^0Fe^{II}, $Cu^{I}Mo^{VI}$) embedded in a protecting, sulphur-rich ligand environment.[18–21]

With CODHs being a role model, numerous homogeneous catalysts for the photocatalytic CO_2 reduction have been developed in the past, though, most of them utilizing only one 3d metal within a macrocyclic chelating ligand.[15,16,22–25] In addition, among the rare bimetallic catalysts like $\mathbf{Co_21}$ or $\mathbf{Ni_21}$ (Scheme 1), geometric constraints do often suppress synergistic catalysis between metal centres.[26,27] One recent example for actual cooperative effects during CO_2 reduction was described by Robert *et al.*[28] Under visible light irradiation, the Co_2 bi-

[a]*Fraunhofer UMSICHT, Osterfelder Str. 3, 46047 Oberhausen, Germany. E-mail: ulf-peter.apfel@umsicht.fraunhofer.de; ulf.apfel@rub.de*

[b]*Institute of Chemistry, Humboldt-Universität zu Berlin, Brook-Taylor Str. 2, 12489 Berlin, Germany*

[c]*Department of Chemistry, Universität Basel, St. Johanns-Ring 19, 4056 Basel, Switzerland*

[d]*Université Paris Cité, Laboratoire d'Electrochimie Moléculaire, CNRS, F-75013 Paris, France*

[e]*Institut Universitaire de France (IUF), F-76006 Paris, France*

[f]*Inorganic Chemistry I, Ruhr-Universität Bochum, Universitätsstr. 150, 44801 Bochum, Germany*

† Electronic supplementary information (ESI) available. See DOI: https://doi.org/10.1039/d3sc02679e

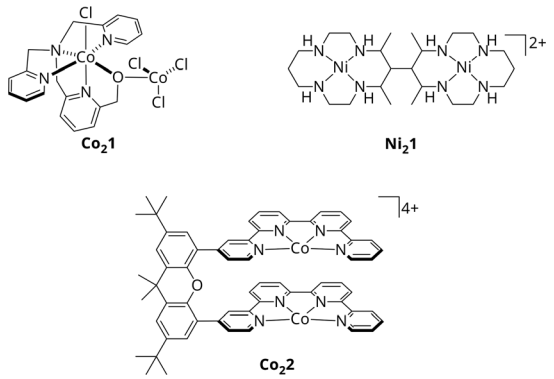

Scheme 1 Molecular structures of $Co_2$1, $Ni_2$1 and $Co_2$2.[26–28]

quaterpyridine complex $\mathbf{Co_2 2}$ (Scheme 1) selectively (max. 97%) reduces CO_2 to formate in basic acetonitrile solution with a turnover frequency (TOF) of 0.23 min^{-1}. Addition of a weak acid such as phenol shifts the reaction to CO with 99% selectivity and an increased catalytic rate of 13.8 min^{-1}. Notably, the product outcome is dependent on the metal-bound η^2 isomer of CO_2, $\eta^2_{O,O}$ or $\eta^2_{C,O}$, stabilised under the respective conditions, leading to either formate or CO. However, in both cases, CO_2 is bound between the Co centres, highlighting the potential of bimetallic complexes.

In the past, we amongst others reported on the ability of dinuclear azacryptates for the uptake of atmospheric CO_2 as bicarbonate between the metal centres including Co_2,[29] Ni_2,[30] Cu_2 [31] or Zn_2 [32] complexes. Beyond these reports, Lu *et al.* reported on a dinuclear Co_2 azacryptate ($\mathbf{Co^{II}Co^{II}}$-$\mathbf{\{N^NN^N\}_m}$, Scheme 2) as photocatalyst for the visible light-driven CO_2 conversion in a water-containing system with $[Ru(phen)_3](PF_6)_2$ as photosensitiser (PS) and triethanolamine (TEOA) as sacrificial electron donor (SED). Due to synergistic effects between the Co^{II} centres, the cryptate was reported to reach a high catalytic rate of 0.47 s^{-1} compared to its mononuclear analogue with 0.04 s^{-1}, while exhibiting a high selectivity of 98% for CO evolution even in the presence of water.[33] The observed cooperativity was even more pronounced, when one Co^{II} was exchanged by Zn^{II} to yield $\mathbf{Zn^{II}Co^{II}}$-$\mathbf{\{N^NN^N\}_m}$, resulting in an enhanced activity for CO_2-to-CO conversion with 1.80 s^{-1} and a maintained high selectivity. Due to the stronger binding affinity of Zn^{II} over Co^{II} to OH^- in the critical C–O cleaving step, C–O bond cleavage is greatly promoted, highlighting the importance of understanding the role of metals in dual CO_2 activation.[34]

These findings pointed our interest towards photocatalysts comprising azacryptates with not only metal centres of different kind but also oxidation states. Especially since the presence of a frustrated Lewis pair is crucial for the reduction of CO_2 within the CODHs, we got interested in cooperative metal–metal effects for CO_2 reduction.[18] Along this line, we recently reported on the synthesis of the asymmetric cryptand $\mathbf{\{N^SN^N\}_m}$ which allows for the site-specific coordination of Cu^I and either Co^{II}, Ni^{II} or Cu^{II} through sulphur incorporation within the ligand framework (Scheme 2). Furthermore, the distance between the metal centres can be increased when using $\mathbf{\{N^SN^N\}_p}$ as ligand.[35]

Thus, we herein report on the photocatalytic activity of $\mathbf{Cu^I Co^{II}}$-$\mathbf{\{N^SN^N\}_m}$ towards CO_2 reduction with additional focus on the influence of the metal distance. The selection of $\mathbf{Cu^ICo^{II}}$-$\mathbf{\{N^SN^N\}_m}$ is based on the following considerations: (1) the Co^{II}-$\{N^N\}$ site was already successfully reported for photocatalytic CO_2 conversion[33,34] and thus, allows for studying alterations of the other catalytic site. (2) Considering the active site's sulphur-rich environment in CO_2-converting enzymes, using a catalyst with sulphur donors was desired. (3) Cu^I-$\{N^S\}$ was synthetically easily accessible due to the matching donor–acceptor properties of Cu^I and sulphur and exhibits structural similarity to the active site of the [MoCu]-CODH.

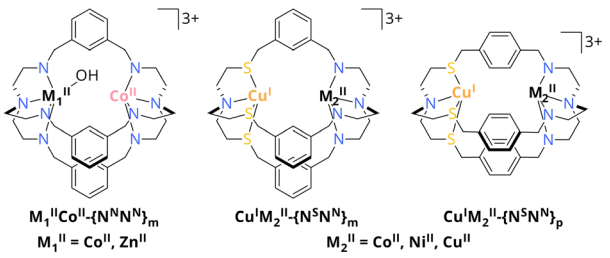

Scheme 2 Schematic overview of $Co^{II}M_1{}^{II}$-$\mathbf{\{N^NN^N\}_m}$ with $M_1{}^{II}$ = Co^{II}, Zn^{II} and $Cu^IM_2{}^{II}$-$\mathbf{\{N^SN^N\}_{m/p}}$ with $M_2{}^{II}$ = Co^{II}, Ni^{II}, Cu^{II}. Hydrogen atoms are omitted for clarity.[32,33]

Results and discussion

In order to investigate the influence of mixed-valent metal centres on the overall CO_2 reduction reactivity, we herein examined the stable heterobimetallic complex $\mathbf{Cu^ICo^{II}}$-$\mathbf{\{N^SN^N\}_m}$ as potential photocatalyst under otherwise similar conditions as was reported by Lu *et al.*[33,35] Like commonly described for bimetallic azacryptates,[31,33,34,36] $\mathbf{Cu^ICo^{II}}$-$\mathbf{\{N^SN^N\}_m}$ readily absorbs CO_2 which is indicated by a change of the UV/vis/NIR spectrum upon purging a MeCN/H_2O (4 : 1) complex solution with CO_2 for 5 min, indeed making it a promising candidate as a CO_2 reduction catalyst. In the presence of CO_2, the absorbance maxima at 490 nm and 618 nm decrease while the absorbance below 378 nm increases, consequently generating an isosbestic point (Fig. S1, ESI†) and thus, indicating the formation of a new species. The presence of a mass peak at m/z = 931.3 in the ESI-MS spectrum matching the $[Cu^ICo^{II}\text{-}\{N^SN^N\}(HCO_3)(ClO_4)]^+$ fragment (Fig. S2B, ESI†) suggests a fixation of CO_2 as bicarbonate. Moreover, the intensification of bicarbonate-related vibrations at 1641 cm^{-1} and 1449 cm^{-1} in the respective IR spectrum (Fig. S2A, ESI†) support this finding, albeit they coincide with ligand-associated vibrations.[31,36,37] Notably, under Ar atmosphere, the UV/vis/NIR spectrum remained unchanged within 24 h and illustrates the high stability of $\mathbf{Cu^ICo^{II}}$-$\mathbf{\{N^SN^N\}_m}$ in solution.

Visible light-driven reduction of CO_2 to CO with $\mathbf{Cu^ICo^{II}}$-$\mathbf{\{N^SN^N\}_m}$ as catalyst

The photocatalytic CO_2 reduction experiments were performed using 2 μM $\mathbf{Cu^ICo^{II}}$-$\mathbf{\{N^SN^N\}_m}$ as catalyst, 0.4 mM

$[Ru(phen)_3](PF_6)_2$ as photosensitizer and 0.3 M triethanolamine (TEOA) as sacrificial reductant in CO_2-saturated MeCN/H_2O (4 : 1) at room temperature. The photosystem was illuminated (450 nm LED, light intensity of 1200 mcd, irradiation area 0.8 cm^2) for 56 h with two-hourly GC-BID analysis (except for hours 14–22 and 36–44) of the headspace composition as well as GC-MS analysis of the liquid phase composition after 56 h. All given values were averaged over three experiments with typical uncertainties of 2–8%. CO was observed as sole carbon-based product from CO_2 reduction (Fig. S3 and S4, ESI†) with a steady increase of evolution during the first 24 h (Fig. 1). Beyond this point, the CO production ceased and the maximum value with 9.22 μM was reached, corresponding to a turnover number (TON) of 2305 and turnover frequency (TOF) of 1.60 min^{-1}. Only H_2 was formed as side product from proton reduction with 0.189 μmol (TON of 47, TOF of 3.28×10^{-3} min^{-1}) after 24 h, leading to a high selectivity of 98% for CO_2-to-CO conversion. Analysis of the liquid phase furthermore revealed the formation of acetaldehyde which can be attributed to the degradation of TEOA.[38] The quantum yield was determined to be 0.15% using a potassium ferrioxalate actinometer (Fig. S5, ESI†). Contrary, in the absence of either $\mathbf{Cu^ICo^{II}}$-$\mathbf{\{N^SN^N\}_m}$, $[Ru(phen)_3](PF_6)_2$, TEOA or in the dark, no CO was detected, thus, showing the necessity of each component for the photocatalytic system (Fig. S6, ESI†). The small activity for H_2 production with 8.85×10^{-3} min^{-1} (0.0510 μmol, TON of 13, 24 h) observed in experiments without $\mathbf{Cu^ICo^{II}}$-$\mathbf{\{N^SN^N\}_m}$ is due to $[Ru(phen)_3](PF_6)_2$ which can also act simultaneously as photosensitiser and catalyst for hydrogen evolution itself.[39,40] Irradiation of an Ar purged solution instead of CO_2 also generated no CO, excluding a potential CO production through degradation of any of the components of the photocatalytic system. Moreover, the presence of the proton source plays a pivotal role as well (Fig. S7, ESI†). While in neat MeCN the CO production rate is with 3.84×10^{-2} min^{-1} low (0.221 μmol, TON of 55, 24 h), addition of water with a ratio of MeCN/H_2O 9 : 1 increased the activity to 1.08 min^{-1} (6.23 μmol CO, TON of 1558, 24 h). The best performance was achieved with the MeCN/H_2O mixture of 4 : 1 while further increase of the water content to 1 : 1 limited the CO production to 1.37×10^{-2} min^{-1} (0.0791 μmol, TON of 20, 24 h). Isotope labelling experiments performed under a $^{13}CO_2$ atmosphere followed by gas chromatography mass spectrometry analysis of the headspace, revealed the formation of ^{13}CO ($m/z = 29$) as reduction product confirming that CO originates from CO_2 (Fig. S8, ESI†).

Since the UV/vis/NIR spectrum of a MeCN/H_2O (4 : 1) solution of 0.6 mM $\mathbf{Cu^ICo^{II}}$-$\mathbf{\{N^SN^N\}_m}$ did not alter during 24 h irradiation, stability of the catalyst under irradiation can be anticipated (Fig. S1, ESI†) which is supported by the continuous production of CO during this time. HPLC analysis of the photocatalytic solution after 24 h irradiation followed by subsequent ESI-MS of the catalyst-containing fraction revealed a signal at $m/z = 478.6$ in the negative mode corresponding to $[Cu^ICo^{II}\text{-}\{N^SN^N\}(BF_4)(ClO_4)(\text{-}3H)]^{2-}$ (Fig. S9, ESI†) and thus, further confirming the integrity of $\mathbf{Cu^ICo^{II}}$-$\mathbf{\{N^SN^N\}_m}$. The durability of the photosystem, however, is limited to 24 h as shown by the ceasing CO production beyond this hour (Fig. 1). Since TEOA is present in large excess and the UV/vis/NIR spectrum of $[Ru(phen)_3](PF_6)_2$ (Fig. S10, ESI†) shows a steady decrease of the absorbance maximum at 446 nm until 24 h, this finding can be attributed to the photodegradation of $[Ru(phen)_3](PF_6)_2$. Furthermore, experiments in the presence of mercury revealed when considering the margins a similar CO production rate with 1.27 min^{-1} (7.34 μmol, TON of 1835, 24 h) and increased H_2 production with 3.72×10^{-2} min^{-1} (0.214 μmol, TON of 54, 24 h) revealing that the catalytic reaction is predominantly homogeneous and does not result from elemental Cu or Co due to catalyst degradation. The absence of any particles in the photocatalytic solution after irradiation for 24 h is further confirmed by particle size analysis using laser diffraction (Fig. S11, ESI†). Consequently, reactivation experiments were performed in which fresh $[Ru(phen)_3](PF_6)_2$ was added to the catalytic system after 26 h and 52 h (Fig. S12, ESI†). Notably, after addition of fresh photosensitiser, the CO production was increased again, achieving similar catalytic rates like after 24 h, with 1.70 min^{-1} (11.4 μmol, TON of 2850) and 1.48 min^{-1} (19.2 μmol, TON of 4800) after 2 h of the first and second re-addition, respectively, ultimately highlighting that $[Ru(phen)_3](PF_6)_2$ is the main limiting factor herein.

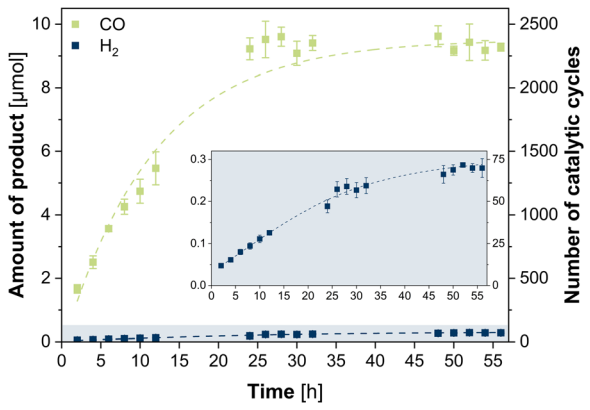

Fig. 1 Photocatalytic evolution of CO (green) and H_2 (blue) during 56 h catalysed by $\mathbf{Cu^ICo^{II}}$-$\mathbf{\{N^SN^N\}_m}$ (2 μM) in a CO_2-saturated MeCN/H_2O (4 : 1) solution containing 0.4 mM $[Ru(phen)_3](PF_6)_2$ and 0.3 M TEOA under irradiation with blue LED light (λ = 450 nm, 1200 mcd, irradiation area 0.8 cm^2). Dashed lines represent the best fit of data.

Synergistic catalysis and influence of metal distance on CO_2 reduction

To explore the ongoing photocatalytic reaction in detail, investigations on the CO evolution kinetics were performed in a first step. Concentration-dependent experiments with 0.5, 1.0, 1.5 and 2 μM catalyst show at every hour a linear dependence of the concentration *versus* the amount of CO generated (Fig. S13, ESI†), suggesting a first-order reaction for the CO_2-to-CO conversion. To consequently gain a more profound insight into the catalytic activity of the individual metals within $\mathbf{Cu^ICo^{II}}$-$\mathbf{\{N^SN^N\}_m}$, we also employed the mononuclear counterparts $\mathbf{Cu^I}$-$\mathbf{\{N^SN^N\}_m}$ and $\mathbf{Co^{II}}$-$\mathbf{\{N^SN^N\}_m}$ as comparative catalyst systems (Fig. 2B).[35] While the CO and H_2 production with $\mathbf{Cu^I}$-$\mathbf{\{N^SN^N\}_m}$

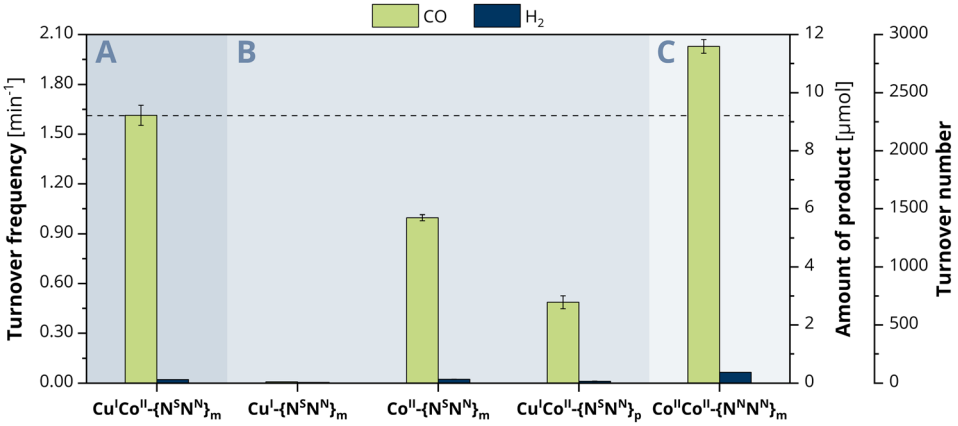

Fig. 2 Photocatalytic evolution of CO (green) and H_2 (blue) after 24 h irradiation with blue LED light ($\lambda = 450$ nm, 1200 mcd, irradiation area 0.8 cm^2) of a CO_2-saturated MeCN/H_2O (4 : 1) solution containing 0.4 mM $[Ru(phen)_3](PF_6)_2$ and 0.3 M TEOA with (A) $\mathbf{Cu^ICo^{II}}$-$\mathbf{\{N^SN^N\}_m}$, (B) $\mathbf{Cu^I}$-$\mathbf{\{N^SN^N\}_m}$, $\mathbf{Co^{II}}$-$\mathbf{\{N^SN^N\}_m}$, and $\mathbf{Cu^ICo^{II}}$-$\mathbf{\{N^SN^N\}_p}$ or (C) $\mathbf{Co^{II}Co^{II}}$-$\mathbf{\{N^NN^N\}_m}$ as catalyst.

was neglectable (CO: 0.01 min^{-1}, 0.0464 µmol, TON of 12, H_2: 4.86×10^{-3} min^{-1}, 0.0279 µmol, TON of 7, 24 h), complex $\mathbf{Co^{II}}$-$\mathbf{\{N^SN^N\}_m}$ achieved a catalytic rate of 0.99 min^{-1} (5.70 µmol, TON 1425, 24 h) for CO and 2.34×10^{-3} min^{-1} (0.135 µmol, TON 34, 24 h) for H_2, corresponding to a 98% selectivity of CO over H_2 production. Thus, the nearly absent activity with Cu and the decreased activity with Co suggest that probably only the Co centre is the redox-active site during catalysis within $\mathbf{Cu^ICo^{II}}$-$\mathbf{\{N^SN^N\}_m}$ but synergistically benefiting from the presence of the Cu centre.

We therefore became curious about whether the CO generation can be influenced by a variation of the metal distance between Cu^I and Co^{II}. We previously described that the distance between the binding sites of the *para*-substituted analogue of the ligand, $\mathbf{\{N^SN^N\}_p}$, is roughly 1 Å larger than in $\mathbf{\{N^SN^N\}_m}$, giving a metal–metal distance of 6.578 Å within the related Cu^ICu^{II} cryptate.[35] Due to the lack of a crystal structure of a corresponding *meta* cryptate, we consequently refer to the distance between the binding sites in the empty ligand and used $\mathbf{Cu^ICo^{II}}$-$\mathbf{\{N^SN^N\}_p}$ as catalyst for comparison. Under otherwise identical conditions, $\mathbf{Cu^ICo^{II}}$-$\mathbf{\{N^SN^N\}_p}$ achieved a CO production rate of 0.48 min^{-1} (2.78 µmol, TON of 695, 24 h) and a H_2 production of 1.17×10^{-2} min^{-1} (0.0671 µmol, TON of 17, 24 h) (Fig. 2B). These values are significantly smaller compared to those observed with $\mathbf{Cu^ICo^{II}}$-$\mathbf{\{N^SN^N\}_m}$ showing that the metal distance within $\mathbf{Cu^ICo^{II}}$-$\mathbf{\{N^SN^N\}_p}$ is too large for synergistic catalysis to occur; therefore, it is possible that the Co^{II} site is solely responsible for the observed activity. Interestingly, $\mathbf{Cu^I Co^{II}}$-$\mathbf{\{N^SN^N\}_p}$ has a smaller activity for CO production than the mononuclear catalyst $\mathbf{Co^{II}}$-$\mathbf{\{N^SN^N\}_m}$. We preliminarily attribute this not only to the altered metal distance but also lowered flexibility of the macrocycle caused by the *para*-substituted spacers bridging the two binding sites.

Mechanistic studies of the CO_2 reduction

Electrochemical investigations. The electrochemical properties of $\mathbf{Cu^ICo^{II}}$-$\mathbf{\{N^SN^N\}_m}$ were determined by cyclic voltammetry (CV) in anhydrous MeCN using 0.1 M tetrabutylammonium hexafluorophosphate ($[^nBu_4N]PF_6$) as supporting electrolyte (Fig. S14A, ESI†). The CV reveals a redox couple at −0.88 V *vs.* $Fc^{+/0}$ under inert conditions which is shifted anodically upon addition of CO_2 to −0.84 V *vs.* $Fc^{+/0}$. No significant increase in current was observed, indicating that in the absence of a proton source, no catalytic transformation of CO_2 is going on. In MeCN/H_2O (4 : 1), $\mathbf{Cu^ICo^{II}}$-$\mathbf{\{N^SN^N\}_m}$ exhibits one primary reduction wave at −1.05 V *vs.* $Fc^{+/0}$ and at −1.59 V *vs.* $Fc^{+/0}$. Overlay with the CVs of the monometallic counterparts $\mathbf{Cu^I}$-$\mathbf{\{N^SN^N\}_m}$ and $\mathbf{Co^{II}}$-$\mathbf{\{N^SN^N\}_m}$ clarifies that the former wave can be assigned to the reduction of Co^{II} to Co^I and the latter one corresponds to the reduction of Cu^I (Fig. S14B, ESI†). The corresponding oxidations for Cu^0 to Cu^I and Co^I to Co^{II} appear at −0.78 and −0.62 V *vs.* $Fc^{+/0}$, respectively. Additionally, the herein measured potential window displays further the oxidation of Cu^I to Cu^{II} at −0.25 V followed by reduction at −0.76 V *vs.* $Fc^{+/0}$. Upon saturation with CO_2, the $Co^{II/I}$ redox couple remains nearly unchanged in terms of current but with a minor anodic shift to −1.01 V. Furthermore, an additional diffusion-limited signal can be observed, suggesting an interaction with CO_2, followed by a catalytic response at higher potentials (Fig. S14C and S15A, ESI†). Contrary, a pre-catalyst transformation was not observed in the linear sweep voltammogram (LSV) of $\mathbf{Co^{II}}$-$\mathbf{\{N^SN^N\}_m}$ in the presence of CO_2 with a catalytic current increase from −1.44 V *vs.* $Fc^{+/0}$, suggesting that it follows a different mechanism than $\mathbf{Cu^ICo^{II}}$-$\mathbf{\{N^SN^N\}_m}$. This is also the case for $\mathbf{Cu^I}$-$\mathbf{\{N^SN^N\}_m}$ which additionally does not display a catalytic response at considerable potential, supporting its inactivity towards the photocatalytic CO_2 reduction. Since the LSVs of $\mathbf{Cu^ICo^{II}}$-$\mathbf{\{N^SN^N\}_m}$ and $\mathbf{Cu^ICo^{II}}$-$\mathbf{\{N^SN^N\}_p}$ show a similar behaviour upon addition of CO_2, no reason for the difference in reactivity within the photocatalytic CO evolution can be drawn from the electrochemical studies (Fig. S15A, ESI†).

Luminescence quenching. Stern–Volmer emission quenching experiments between the excited state of the photosensitiser $[Ru(phen)_3]^{2+*}$ and either $\mathbf{Cu^ICo^{II}}$-$\mathbf{\{N^SN^N\}_m}$ or TEOA revealed quenching rate constants of 4.13×10^7 M^{-1} s^{-1} and 3.37×10^4 M^{-1} s^{-1}, respectively (Fig. S16 and S17, ESI†). Under

experimentally relevant conditions, the reaction between triplet excited $[Ru(phen)_3]^{2+}$* and TEOA ($k_{TEOA} = 1.01 \times 10^4$ s^{-1}) is roughly a factor of 120 faster than the reaction between $[Ru(phen)_3]^{2+}$* and **Cu^{I}Co^{II}-{N^{S}N^{N}}$_{m}$** ($k_{Cat} = 82.6$ s^{-1}). Thus, electron transfer occurs firstly from TEOA to the excited photosensitiser and subsequently from $[Ru(phen)_3]^{+}$ to the catalyst. The electrochemical studies support that this electron transfer is thermodynamically accessible since the standard redox potential of $[Ru(phen)_3]^{2+/+}$ (−1.77 V *vs.* $Fc^{+/0}$, Fig. S18, ESI†) is more negative than all redox couples determined for **Cu^{I}Co^{II}-{N^{S}N^{N}}$_{m}$**. However, electron transfer to Co^{II} should be more likely than reduction of Cu^{I} due to its less cathodic reduction potential of −1.01 V compared to −1.54 V *vs.* $Fc^{+/0}$, respectively.

Computational studies. The synergistic catalysis between Cu^{I} and Co^{II} in the given coordination environments has been further investigated by computational calculations and a reaction pathway for the CO_2-to-CO conversion by **Cu^{I}Co^{II}-{N^{S}N^{N}}$_{m}$** was proposed (Scheme 3 and Fig. S19, ESI†). Prior to any mechanistic study, the binding energies of potential axial ligands including CO_2, MeCN, OH^- and CO with respect to ligation of the unreduced catalyst were computed and the hydroxyl anion was found to bind strongest. Since it is well known that the fixation of CO_2 within bimetallic cryptates proceeds *via* hydroxo species as bicarbonate in basic solution, the hydroxylated catalyst **CuCo1** that accommodates OH^- at the Co^{II}-{N^{N}} site is a reasonable starting point.[31–34,36,37] Consequently, CO_2 uptake results in the formation of the $\mu_2,\eta^2_{O,O}$ bicarbonate adduct **CuCo2** with 6.9 kcal mol^{-1} reaction free energy, resulting from the cage-deformation upon binding of the ligand. This step is in good agreement with the aforementioned results from IR spectroscopy and mass spectrometry which suggested an incorporated bicarbonate ligand within **Cu^{I}Co^{II}-{N^{S}N^{N}}$_{m}$** in the presence of CO_2. Subsequently, an exothermic proton-coupled electron transfer (PCET) accompanied by the release of water yields the Co^{I}–CO_2 complex **CuCo3**. Here, the spin density is entirely located at the Co^{I} centre and electron transfer to the lowest unoccupied molecular orbital (LUMO) of CO_2 has not yet occurred which is reflected by its almost linear structure ($\angle = 176.7°$). Upon intramolecular electron transfer with a reaction free energy of 6.0 kcal mol^{-1} and energy barrier of 8.8 kcal mol^{-1}, the CO_2 radical anion is formed *via* transition state **CuCo-TS1** which is accompanied by a reduction of the O–C–O angle and a change in binding mode from terminal to μ_2,η^3 (**CuCo4**). A further PCET yields the $\mu_2,\eta^2_{C,O}$ Co-COOH-Cu complex **CuCo5** with the hydroxy moiety still weakly bound to the Cu centre. Subsequent C–OH bond cleavage *via* transition state **CuCo-TS2** results in **CuCo6** with Co-bound CO and Cu-bound OH^-. Although a further reduction of the Co$^{II/I}$–CO couple is favourable in terms of redox potential and binding energy of CO to cobalt (Tables S1 and S2, ESI†), the interaction between the two intracavitary ligands is rather unfavourable with a predicted energy barrier of 8.9 kcal mol^{-1}. Thus, the following highly exothermic release of CO (−28.8 kcal mol^{-1}) to yield **CuCo7** together with the continuous mass transport of gaseous CO, is the driving force for this reaction step and preferred over a further reduction (+14.4 kcal mol^{-1}). After migration of the hydroxyl group to the Co centre with an energy barrier of 7.1 kcal mol^{-1}, the initial catalyst is restored, and the catalytic cycle can restart.

A comparison of the catalytic cycle with the experimental results of the mononuclear analogues reveals a good agreement of the predictions of the role of the individual metal within **Cu^{I}Co^{II}-{N^{S}N^{N}}$_{m}$**. The nearly absent activity of **Cu^{I}-{N^{S}N^{N}}$_{m}$** towards the reduction of CO_2 is in line with Cu taking over an assistant role in binding during catalysis. In contrast, Co was experimentally proposed as redox-active site due to the activity of **Co^{II}-{N^{S}N^{N}}$_{m}$** towards CO_2-to-CO conversion which matches the role of Co during the catalytic cycle, too. To further strengthen these findings, smaller computed scaffold models comprising the specific tripodal ligand backbone with an open coordination site in axial position (Fig. S20, ESI†) were considered.[33] While one-electron reduction of the Cu^{I}-{N^{S}} site alone entails a complex decomposition, addition of an electron to Cu^{I}-{N^{S}} and CO_2 leads to the formation of the $CO_2^{\bullet-}$ that is only weakly bound to the catalyst ($d = 2.83$ Å). Hence, in accordance with the experimental results for **Cu^{I}-{N^{S}N^{N}}$_{m}$**, a pathway for the reaction between Cu^{I}-{N^{S}} and CO_2 could not be established. Contrary to Cu^{I}-{N^{S}} and thus, in good agreement with the experimental results for **Co^{II}-{N^{S}N^{N}}$_{m}$**, a reaction profile for the Co^{II}-{N^{N}} site with CO_2 was proposed by Lu *et al.*[33] Therein, a simultaneous two-electron transfer step from the Co centre to CO_2 yields a η^1_C Co^{III}–CO_2^{2-} intermediate which is transformed in a PCET into Co^{II}-COOH$^-$. Subsequently, C–OH bond cleavage results in CO and OH^-, both bound to Co, followed by release of the former. While the simultaneous two-electron reduction of CO_2 in Co^{II}-{N^{N}} proceeds with an energy barrier of 19.5 kcal mol^{-1},[33] the one for the stepwise reduction in **Cu^{I}Co^{II}-**

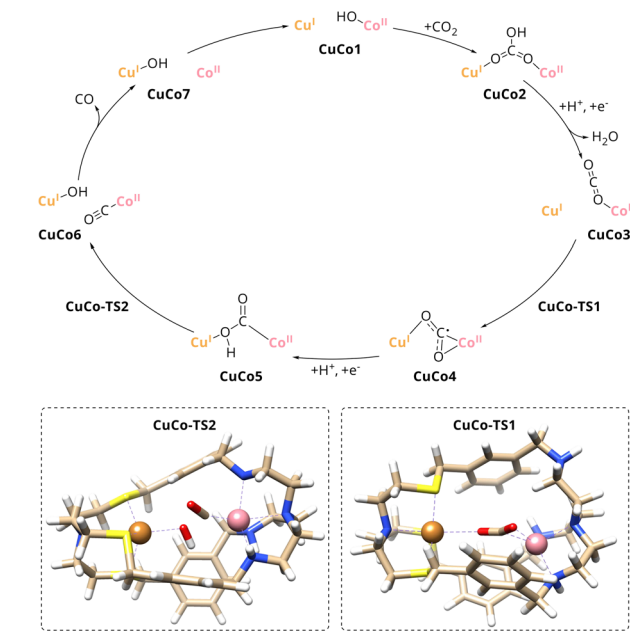

Scheme 3 Proposed mechanism for CO_2 reduction to CO with **Cu^{I}Co^{II}-{N^{S}N^{N}}$_{m}$** as catalyst. (Inset) Transition state structures for one electron CO_2 reduction and C–OH bond cleavage, **CuCo-TS1** and **CuCo-TS2**, respectively.

$\{N^SN^N\}_m$ with 10.4 kcal mol^{-1} is significantly lower which is which most likely due to the favourable interaction of Cu stabilising the $CO_2^{\bullet-}$ adduct in **CuCo4**. Furthermore, the energy barrier of the following C–OH bond cleavage is considerably lower for Cu^ICo^{II}-$\{N^SN^N\}_m$ (8.9 kcal mol^{-1}) compared to the reported value for the mononuclear case (18.1 kcal mol^{-1}).[33] Consequently, benefitting from the synergistic effect between the two metals, with Co^{II} as active site and Cu^I taking over an assistant role in binding, CO_2 reduction to CO is more favoured in the dinuclear cryptate Cu^ICo^{II}-$\{N^SN^N\}_m$.

The computed binding mode of the CO_2 radical anion for the *meta* and *para* analogue of the Cu^ICo^{II} complex (Fig. 3 and S21, ESI†) also supports the significantly lowered activity of Cu^ICo^{II}-$\{N^SN^N\}_p$. While the distance between the binding sites in $\{N^SN^N\}_m$ is inherently smaller,[35] it exhibits a higher flexibility and the corresponding metal complex can consequently adapt an even smaller bite length in the presence of various substrates (Table S3, ESI†). For example, owing to the flexible nature of Cu^ICo^{II}-$\{N^SN^N\}_m$, the Cu–Co distance reduces from 6.20 to 4.60 Å for the accommodation of the CO_2 radical anion, affording a dual $\mu_2,\eta^2_{C,O}$ binding mode. In contrast, the lowered flexibility of Cu^ICo^{II}-$\{N^SN^N\}_p$ only allows for a deviation of the metal distance by 0.19 Å, binding the $CO_2^{\bullet-}$ *via* its two oxo sites in a $\mu_2,\eta^2_{O,O}$ fashion, consequently preventing synergistic catalysis.

Comparison with the octa-amino, homodinuclear cryptate $Co^{II}Co^{II}$-$\{N^NN^N\}$

To classify the activity of Cu^ICo^{II}-$\{N^SN^N\}_m$ and compare it with $Co^{II}Co^{II}$-$\{N^NN^N\}_m$ described by Lu *et al.*,[34] we prepared the full-nitrogen system according to the described procedure and tested it as photocatalyst for the CO_2 reduction under the herein stated conditions with 2 μM catalyst concentration. Small deviations within the photosystem set-up compared to the one used in literature might lead to a great difference in product outcome and make a direct comparison of the results difficult. In the herein employed photosystem, $Co^{II}Co^{II}$-$\{N^NN^N\}_m$ achieved a production rate of 2.01 min^{-1} (11.6 μmol, TON of 2900, 24 h) and 6.51 × 10^{-2} min^{-1} (0.375 μmol, TON of 94, 24 h) for CO and H_2, respectively, corresponding to a 97% selectivity for CO_2-to-CO conversion (Fig. 2C). Notably, the activity of Cu^ICo^{II}-$\{N^SN^N\}_m$ towards CO_2-to-CO conversion is with 1.60 min^{-1} smaller with a maintained selectivity over H_2 production as with $Co^{II}Co^{II}$-$\{N^NN^N\}_m$. Although Cu^ICo^{II}-$\{N^SN^N\}_m$ allows for the reduction of Co^{II} to Co^I at more anodic potential (−1.01 V *vs.* $Fc^{+/0}$) compared to $Co^{II}Co^{II}$-$\{N^NN^N\}_m$ (−1.15 V *vs.* Fc^{+0}, one electron reduction to Co^ICo^{II}[33]), the LSV of the latter shows a drastic increase of current upon CO_2 saturation after the Co^{II} reduction wave (Fig. S11B, ESI†). For Cu^ICo^{II}-$\{N^SN^N\}_m$, a similar current is only observed at roughly 0.4 V more cathodic potentials, providing one reason for the lower activity compared to $Co^{II}Co^{II}$-$\{N^NN^N\}_m$. Although a comparison of the proposed reaction mechanisms for the CO_2-to-CO conversion with Cu^ICo^{II}-$\{N^SN^N\}_m$ and the previously described $Co^{II}Co^{II}$-$\{N^NN^N\}_m$ reveal that they follow different pathways for the actual reduction of CO_2, the critical C–OH bond cleaving step is similar for both.[33] Here, the assisting binding site, Cu^I-$\{N^S\}$ or Co^{II}-$\{N^N\}$ in case of Cu^ICo^{II}-$\{N^SN^N\}_m$ and $Co^{II}Co^{II}$-$\{N^NN^N\}_m$, respectively, plays an important role. Since Cu^I-$\{N^S\}$ exhibits a higher electron density compared to Co^{II}-$\{N^N\}$, the binding affinity to the negatively charged OH^- is less pronounced. Thus, bond cleavage is promoted to a lower extent, consequently resulting in the lower activity of Cu^ICo^{II}-$\{N^SN^N\}_m$. Furthermore, next to the synergistic pathway in $Co^{II}Co^{II}$-$\{N^NN^N\}_m$, single-sited catalysis at both Co centres individually is conceivable as well, considerably enhancing the chance for CO_2 reduction to occur. Due to the inactivity of the single Cu^I-$\{N^S\}$ site, this is not the case for Cu^ICo^{II}-$\{N^SN^N\}_m$.

At this point, we became curious on investigating the effect of incorporating two Co^{II} into $\{N^SN^N\}_m$ on the photocatalytic CO_2 reduction. Experiments with $Co^{II}Co^{II}$-$\{N^SN^N\}_m$ however, revealed lower catalytic rates for CO_2-to-CO conversion with 1.11 min^{-1} (6.39 μmol, TON of 1598, 24 h) compared to both, $Co^{II}Co^{II}$-$\{N^NN^N\}_m$ and Cu^ICo^{II}-$\{N^SN^N\}_m$. Same was for $Zn^{II}Co^{II}$-$\{N^SN^N\}_m$ with 1.08 min^{-1} (6.21 μmol, TON of 1553, 24 h), despite the significantly improved catalysis observed for the corresponding $Zn^{II}Co^{II}$ complex of the full-nitrogen system $\{N_NN_N\}_m$.[34] Interestingly, the second metal seemingly does not promote the catalysis at all, since the observed rates are in the similar range as for monometallic Co^{II}-$\{N^SN^N\}_m$ (0.99 min^{-1}). The decreased catalytic rates and formation of a precipitate during irradiation together with a few reports on +II metal complexes revealing decreased activity for CO_2-to-CO conversion or tendency to demetallation upon directs N/S exchange in the ligand under reductive conditions,[41–43] let us to the conclusion that the lowered activity is due to decomposition of the $\{N^S\}$ site and consequently emphasises the importance of matching donor–acceptor properties of ligand and metal.

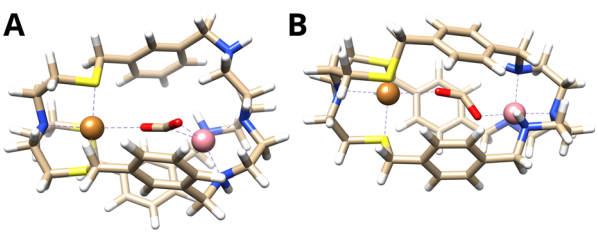

Fig. 3 Binding mode of the CO_2 radical anion within (A) Cu^ICo^{II}-$\{N^SN^N\}_m$ and (B) Cu^ICo^{II}-$\{N^SN^N\}_p$.

Experimental

General techniques

$\{N^SN^N\}_m$ and $\{N^SN^N\}_p$ as well as the corresponding metal complexes Cu^I-$\{N^SN^N\}_m$, Co^{II}-$\{N^SN^N\}_m$, Cu^ICo^{II}-$\{N^SN^N\}_m$ and Cu^ICo^{II}-$\{N^SN^N\}_p$ were synthesized according to a procedure developed previously within our group.[35] For additional characterisation of the beforehand mentioned complexes, CHN experiments were measured with an Elementar vario MICRO cube. $Co^{II}Co^{II}$-$\{N^NN^N\}_m$ was synthesised according to a literature-known procedure.[33] Mass spectra were measured on a Advion expression^L instrument. IR measurements were performed on a Shimadzu IRTracer-100 attached with a Pike

Miracle ATR unit and are reported in [cm^{-1}]. UV/Vis/NIR spectra were recorded with a Shimadzu UV 1900i at 25 °C and are reported in [nm]. X-Band EPR spectra were recorded on a Bruker EMXplus X-band EPR spectrometer. Samples were frozen using a liquid helium recirculating cooling system provided by ColdEdge and were measured at 13 K. The solution in the tube was frozen in liquid nitrogen and kept frozen until measured. ^{1}H NMR spectra for application of Evans' method were obtained on a Bruker DRX 400 MHz NMR spectrometer at room temperature in deuterated acetonitrile (MeCN-d_3), followed by evaluation according to a literature-known procedure. The calculated spin-only effective moment was using the following equation

$$\mu_{eff} = g\sqrt{n(S_{Co}(S_{Co}+1))} \quad (1)$$

with n = number of Co^{II} centres, gyromagnetic ratio $g = 2.00003$ μ_B and spin at Co $S_{Co} = 3/2$ for hs Co^{II}.[44–46]

CHN analysis

$Cu^{I}Co^{II}$-{$N^{S}N^{N}$}$_m$. Anal. calcd for [$C_{36}H_{51}BCl_2CoCuF_4N_5O_8S_3$] + 2 MeOH: C 40.67, H 5.30, N 6.24; found: C 41.32, H 5.31, N 6.34.

Cu^{I}-{$N^{S}N^{N}$}$_m$. Anal. calcd for [$C_{36}H_{51}BCuF_4N_5S_3$] $3H_2O$ + 3 DCM: C 42.23, H 5.73, N 6.31; found: C 42.15, H 5.58, N 6.64.

Co^{II}-{$N^{S}N^{N}$}$_m$. Anal. calcd for [$C_{36}H_{51}Cl_2CoN_5O_8S_3$] + DCM + $2.5H_2O$: C 42.82, H 5.63, N 6.75; found: C 42.83, H 5.37, N 6.62.

$Cu^{I}Co^{II}$-{$N^{S}N^{N}$}$_p$. Anal. calcd for [$C_{36}H_{51}BCl_2CoCuF_4N_5O_8S_3$] + 2.5 MeOH + $0.5H_2O$: C 40.31, H 5.45, N 6.10; found: C 40.95, H 5.34, N 5.93.

Synthesis of $Co^{II}Co^{II}$-{$N^{S}N^{N}$}$_m$

{$N^{S}N^{N}$}$_m$ (34.9 mg, 53.7 μmol) was dissolved in minimum amount of DCM. MeCN/MeOH (4 : 1) was added (2.5 mL), followed by the addition of $Co(ClO_4)_2 \cdot 6H_2O$ (39.3 mg, 107 μmol) dissolved in 0.5 mL MeCN/MeOH (4 : 1) whereupon a direct colour change to brown was observed. The solution was stirred at room temperature for 24 h. Subsequently, the solvent was removed, the residue taken up in MeCN and filtered through a short silica column. After removal of the solvent, **[$Co^{II}Co^{II}${$N^{S}N^{N}$}$_m$][ClO_4)$_4$** (**$Co^{II}Co^{II}$-{$N^{S}N^{N}$}$_m$**) was obtained as a brown solid in 85% (53.2 mg, 45.6 μmol). ESI-MS: calcd for [$Co^{II}Co^{II}$-{$N^{S}N^{N}$}$_m$(-3H)(MeCN)(OH)(Na)]$^+$ m/z = 845.2; found: 844.9. Anal. calcd for [$C_{36}H_{51}Cl_4Co_2N_5O_{16}S_3$] + 0.8 MeCN + $8H_2O$ + 2 DCM: C 31.45, H 4.89, N 5.37; found: C 31.67, H 4.70, N 5.43. IR (ATR): $\tilde{\nu}$ = 3458, 3254, 2943, 2318, 2291, 1638, 1450, 1367, 1101, 930, 802 cm^{-1}. UV/vis/NIR (MeCN): λ_{max} (ε in L mol^{-1} cm^{-1}) = 384 (202 ± 2), 480 (114 ± 3), 587 (54 ± 1) nm. EPR (MeCN, 13 K): $g = 4.29$ (hs Co^{II}).[47] Evans method (MeCN-d_3, 298 K): calcd for two hs Co^{II} $\mu_{eff} = 5.48$ μ_B; exp.: 5.64 μ_B.

Synthesis of $Zn^{II}Co^{II}$-{$N^{S}N^{N}$}$_m$

{$N^{S}N^{N}$}$_m$ (35.0 mg, 53.8 μmol) was dissolved in minimum amount of DCM. MeCN/MeOH (4 : 1) was added (2.5 mL), followed by the addition of $Co(ClO_4)_2 \cdot 6H_2O$ (19.7 mg, 53.8 μmol) dissolved in 0.5 mL MeCN/MeOH (4 : 1) whereupon a direct colour change to light blue was observed. The solution was stirred at room temperature for 24 h. Subsequently, $Zn(ClO_4)_2 \cdot 6H_2O$ (20.1 mg, 53.8 μmol) dissolved in 0.5 mL MeCN/MeOH (4 : 1) was added. Upon addition, the colour changed to beige and it was stirred at room temperature for 24 h. The solvent was removed, the residue taken up in MeCN and filtered through a short silica column. After removal of the solvent, **[$Zn^{II}Co^{II}${$N^{S}N^{N}$}$_m$][ClO_4)$_4$** (**$Zn^{II}Co^{II}$-{$N^{S}N^{N}$}$_m$**) was obtained as a beige solid in 76% (47.9 mg, 40.9 μmol). ESI-MS: calcd for [**$Zn^{II}Co^{II}$-{$N^{S}N^{N}$}$_m$**(ClO_4) (-2H)(MeCN)(Na)]$^+$ m/z = 933.1; found: 933.0; [**$Zn^{II}Co^{II}$-{$N^{S}N^{N}$}$_m$**(ClO_4)(-H)(MeCN)(Na)(Li)]$^+$ m/z = 941.1; found: 940.5; [**$Zn^{II}Co^{II}$-{$N^{S}N^{N}$}$_m$**($2ClO_4$)(-2H)(Li)]$^+$ m/z = 975.1; found: 975.9; calcd for [**$Zn^{II}Co^{II}$-{$N^{S}N^{N}$}$_m$**($4ClO_4$)(H_2O)]$^+$ m/z = 1089.5; found: 1088.8. Anal. calcd for [$C_{36}H_{51}Cl_4CoN_5O_{16}S_3Zn$] + 1.5 MeCN + $6H_2O$ + 2 DCM: C 32.58, H 4.77, N 6.02; found: C 32.25, H 4.54, N 6.11. IR (ATR): $\tilde{\nu}$ = 3460, 3246, 2941, 2317, 2290, 1637, 1450, 1365, 1098, 930, 802 cm^{-1}. UV/vis/NIR (MeCN): λ_{max} (ε in L mol^{-1} cm^{-1}) = 380 (163 ± 6), 480 (57 ± 7), 571 (25 ± 6) nm. EPR (MeCN, 13 K): $g = 4.37$ (hs Co^{II}).[47] Evans method (MeCN-d_3, 298 K): calcd for one hs Co^{II} $\mu_{eff} = 3.87$ μ_B; exp.: 3.17 μ_B.

Photochemistry

The photocatalytic reduction of CO_2 was performed at 25 °C in a 12 mL reactor sealed with a rubber septum containing 2 mL of the catalyst (0.5–2 μM), 0.4 mM [$Ru(phen)_3$](PF_6)$_2$ as photosensitizer and 0.3 M TEOA as sacrificial electron donor in degassed MeCN or MeCN/H_2O (9 : 1, 4 : 1 or 1 : 1 mixtures). The solution was saturated with either Ar, $^{12}CO_2$ or $^{13}CO_2$ and was illuminated with blue LED light (λ = 450 nm, 1200 mcd, 0.8 cm^2 irradiation area) for minimum 24 h and maximum 56 h. For measurements in the absence of light, the reaction was performed in a black chamber. To identify the composition of the gas phase, 50 μL of the headspace were analysed two-hourly by GC-BID *via* hand injection. To analyse the generated liquid products after photocatalysis, 1 mL of the solution was acidified with 100 μL conc. H_2SO_4 and analysed *via* headspace GC-MS (Fig. S3, ESI†). To verify the absence of formate/formic acid, the liquid phase was further analysed for propyl formate after derivatisation with *n*-propanol. Therefore, 400 μL sample were treated with 500 μL *n*-propanol and 100 μL *p*-toluene sulfonic acid and analysed *via* headspace GC-MS (Fig. S4, ESI†). Each photocatalytic reaction was repeated at least three times to confirm the reliability of the data. A summary of the determined data can be found in the ESI (Table S4†).

Determination of quantum yield

The quantum yields of the photocatalytic CO_2 reduction experiments were determined using the equation

$$\Phi_{CO} = \frac{2 \times \text{product molecules}}{\text{incident photons}} \times 100\% \quad (2)$$

where the product molecules were quantified using a calibrated GC-MS or GC-BID system and the number of incident photons was determined using potassium ferrioxalate ($K_3[Fe^{III}(C_2O_4)_3]$) as chemical actinometer at 25 °C.[48] Accordingly, the photon flux was determined to be 8.92×10^{16} s^{-1}.

Quantification of CO_2RR products

Quantification of the headspace gas composition of the photochemical cell was performed using a Shimadzu GC-2010 Pro equipped with a Shimadzu BID-2010 Plus barrier discharge ionization detector (BID). Gas phase separation was performed *via* hand injection using a SPL injector and a Carboxen 1010 PLOT fused silica capillary GC column (L × I.D. 30 m × 0.32 mm, average thickness 15 μm). Solvents were cut off previously with a SH-Rxi-1ms fused silica capillary GC column (L × I.D. 30 m × 0.32 mm, average thickness 1.0 μm) and were deflected to a second detector (TCD). Helium was used as carrier gas. The following gaseous products/components were assayed *via* the GC-BID system: H_2, O_2, N_2, CO, CH_4, C_2H_4, C_2H_6. Quantification of the liquid phase composition of the photochemical cell was performed using a Shimadzu GCMS-QP2020 system equipped with a MS detector. Phase separation was performed *via* headspace analysis using a SH-Rtx-200 ms fused silica capillary GC column (L × I.D. 30 m × 0.25 mm, average thickness 1 μm). Helium was used as carrier gas. The following liquid products/components were assayed *via* the GCMS system: methanol, ethanol, propanol, formate/formic acid, acetate/acetic acid, propionate/propionic acid, acetaldehyde and propionaldehyde. The given values are averaged over three experiments with typical uncertainties of ±2–8%.

High-performance liquid chromatography

Analytical HPLC was performed using a Knauer Smartline setup with a four-wavelength detector and a dynamic mixing chamber with reversed-phase chromatography column (Nucleodur C4 gravity, 5 μm, 125 × 4 mm, flow rate 1 mL min^{-1}). MiliQ-water with 0.1% trifluoroacetic acid (buffer A) and MeCN with 0.1% trifluoroacetic acid (buffer B) were used as eluents. For the analysis, a linear gradient from 99% to 1% buffer A was driven over 15 min.

Particle size measurement

Particle sizes were measured using a Shimadzu SALD-2300 laser diffraction particle size analyzer equipped with a SALD-BC23 Batch cell. Therefore, 1 mL of the irradiated photocatalytic solution was added to the measurement cell containing 12 mL MeCN/H_2O (4 : 1). The obtained particle sizes were calculated using the Fraunhofer approximation.

Electrochemistry

The electrochemical studies were performed using a PalmSens3 or a PalmSens4 potentiostat in a standard three-electrode setup. A glassy carbon electrode was used as working electrode (WE), an Ag wire as pseudo-reference electrode (PRE) and a Pt wire as counter electrode (CE). The working electrode was prepared by successive polishing with 1.0 and 0.3 μm sandpaper and subsequent sonication in MeCN for 10 min. Tetrabutylammonium hexafluorophosphate ($[^nBu_4N]PF_6$, 0.1 M) was used as electrolyte in all electrochemical measurements either in anhydrous MeCN or a mixture of MeCN/H_2O (4 : 1). Prior to each experiment, the electrochemical cell was degassed with Ar for 10 min and an Ar or CO_2 atmosphere was maintained throughout the measurement. All cyclic voltammograms were recorded at a scan rate of 100 mV s^{-1} and after every experiment all pseudo-referenced potentials were referenced against the ferrocenium/ferrocene couple ($Fc^{+/0}$).

Luminescence quenching

Luminescence lifetimes were measured on an Edinburgh Instruments Lifespec II spectrometer with a 472 nm pulsed diode laser (pulse width 75.5 ps).

Computational studies

All reported calculations were carried out with ORCA program package in its version 5.0.3.[49] The meta-hybrid TPSSh functional[50] in conjunction with the ZORA-def2-TZVP(-f) basis set[51] was used during geometry optimisations and final energy evaluations. Grimme's semiempirical van der Waals corrections with the Becke-Johnson damping (D3BJ) were employed to describe dispersive and non-covalent interactions. Scalar relativistic effects were approximated through the zeroth order regular approximation (ZORA).[52–54] The resolution-of-identity (RI) along with chain-of-spheres algorithms (COSX) were used during the SCF cycles to accelerate the computation of two-electron integrals, while utilising the SARC/J basis set for the former approximation as an auxiliary basis.[55–60] Solvent effects were incorporated implicitly within the Conductor-like Polarizable Continuum Model (C-PCM).[61,62] All structures were fully optimised without symmetry constraints. Normal mode analysis was performed for all reported structures to identify the nature of the ground state and transition state structures. Free energies were reported in kcal mol^{-1} at 1 atm and 298 K. An electrode potential was applied by adding $-e\Phi$ with a value of Φ = 1.12 V to the electronic energy for each added electron. The Gibbs free energy of a proton in acetonitrile was taken to be −260.2 kcal mol^{-1}.

Conclusions

In summary, we herein describe $\mathbf{Cu^ICo^{II}}$-$\mathbf{\{N^SN^N\}_m}$ as efficient catalyst for the visible light-driven reduction of CO_2 achieving a CO production rate of 1.60 min^{-1} with a high selectivity of 98% over H_2 production. While $\mathbf{Cu^ICo^{II}}$-$\mathbf{\{N^SN^N\}_m}$ is a stable, homogeneous catalyst, the photosystem durability is limited to 24 h due to photosensitiser degradation, but can be reactivated through addition of new $[Ru(phen)_3](PF_6)_2$. Experiments with the mononuclear analogues of $\mathbf{Cu^ICo^{II}}$-$\mathbf{\{N^SN^N\}_m}$ clearly reveal that the simultaneous presence of both metals has a beneficial influence on the amount of CO produced. While with $\mathbf{Cu^I}$-$\mathbf{\{N^SN^N\}_m}$ nearly no CO_2 reduction was observed, $\mathbf{Co^{II}}$-$\mathbf{\{N^SN^N\}_m}$ produced CO but exhibits a smaller activity than the dinuclear cryptate (0.99 min^{-1}). Computational studies revealed that in case of $\mathbf{Co^{II}}$-$\mathbf{\{N^SN^N\}_m}$ single Co^{II}-sited catalysis is responsible for CO_2 reduction and that the higher activity with $\mathbf{Cu^ICo^{II}}$-$\mathbf{\{N^SN^N\}_m}$ is indeed based on synergistic effects between Cu and Co. Furthermore, experimental and computational studies with $\mathbf{Cu^ICo^{II}}$-$\mathbf{\{N^SN^N\}_p}$ as catalyst show that the increased bite length

together with the decreased flexibility of the *para*-substituted cryptand prevent synergistic CO_2 reduction, thus leading to a significantly smaller catalytic rate. Moreover, compared to $\mathbf{Co^{II}Co^{II}\text{-}\{N^{N}N^{N}\}_m}$, the exchange of one Co^{II}-$\{N^{N}\}$ site by Cu^{I}-$\{N^{S}\}$ in $\mathbf{Cu^{I}Co^{II}\text{-}\{N^{S}N^{N}\}_m}$ is accompanied by a slight decrease in activity due to the smaller binding affinity of the Cu^{I}-$\{N^{S}\}$ site to OH^- which is especially important in the critical C–OH cleaving step. The herein presented results thus provide important insight into the design of bimetallic catalysts and highlight the importance of the interplay of the metal distance as well as binding strength to CO_2 for an efficient C–O bond cleavage and synergistic catalysis.

Data availability

Supplemental figures, tables and relevant data including Cartesian coordinates of all computationally investigated structures have been provided in the ESI.†

Author contributions

J. J. planned and performed synthesis and characterisation of the catalysts, photocatalytic and electrochemical experiments, degradation studies and prepared the original manuscript. E. B. B. carried out all theoretical computations and was involved in writing the manuscript. J. W. performed the luminescence quenching experiments. O. S. W. supervised the luminescence quenching experiments and revised the manuscript. Ma. R. aided in interpreting the results and planning of photocatalytic experiments and revised the manuscript. Mi. R. conceived and supervised all theoretical calculations and was involved in the writing of the manuscript. U.-P. A. conceived the whole research, supervised photocatalytic experiments and finalised the manuscript.

Conflicts of interest

There are no conflicts to declare.

Acknowledgements

This work was supported by the Deutsche Forschungsgemeinschaft (DFG; German Research Foundation) for financial support under Germany's Excellence Strategy – EXC-2033 390677874 – "RESOLV" & AP242/9-1. This work was further supported by the Fraunhofer Internal Programs under Grant no. Attract 097-602175. J. J. gratefully acknowledges financial support from the Deutsche Bundesstiftung Umwelt. E. B. B. and Mi. R. thank the Deutsche Forschungsgemeinschaft for funding through Emmy-Noether project 5688/1. Partial financial support to Ma. R. from the Institut Universitaire de France (IUF) and from ANR (Agence Nationale de la Recherche, ANR-20-SODR-0003-02) is also gratefully acknowledged.

References

1 H. B. Gray, *Nat. Chem.*, 2009, **1**, 7.
2 L. Hammarström, *Acc. Chem. Res.*, 2009, **42**, 1859–1860.
3 J. Barber, *Solar Fuels and Photosynthesis*, Royal Society of Chemistry, London, 2012.
4 Z. Wang, H. Song, H. Liu and J. Ye, *Angew. Chem., Int. Ed.*, 2020, **59**, 8016–8035.
5 J. Strunk, *Heterogeneous Photocatalysis – From Fundamentals to Applications in Energy Conversion and Depollution*, Wiley-VCH, Weinheim, Germany, 2021.
6 H. Shen, T. Peppel, J. Strunk and Z. Sun, *Sol. RRL*, 2020, **4**, 1900546.
7 E. V. Kondratenko, G. Mul, J. Baltrusaitis, G. O. Larrazábal and J. Pérez-Ramírez, *Energy Environ. Sci.*, 2013, **6**, 3112–3135.
8 M. Dilla, R. Schlögl and J. Strunk, *ChemCatChem*, 2017, **9**, 696–704.
9 R. Francke, B. Schille and M. Roemelt, *Chem. Rev.*, 2018, **118**, 4631–4701.
10 F. Möller, S. Piontek, R. G. Miller and U.-P. Apfel, *Chem.–Eur. J.*, 2018, **24**, 1471–1493.
11 J. Bonin, A. Maurin and M. Robert, *Coord. Chem. Rev.*, 2017, **334**, 184–198.
12 K. J. Lee, N. Elgrishi, B. Kandemir and J. L. Dempsey, *Nat. Rev. Chem*, 2017, **1**, 0039.
13 S. Berardi, S. Drouet, L. Francàs, C. Gimbert-Suriñach, M. Guttentag, C. Richmond, T. Stoll and A. Llobet, *Chem. Soc. Rev.*, 2014, **43**, 7501–7519.
14 Y. Pellegrin and F. Odobel, *C. R. Chim.*, 2017, **20**, 283–295.
15 K. E. Dalle, J. Warnan, J. J. Leung, B. Reuillard, I. S. Karmel and E. Reisner, *Chem. Rev.*, 2019, **119**, 2752–2875.
16 E. Boutin, L. Merakeb, B. Ma, B. Boudy, M. Wang, J. Bonin, E. Anxolabéhère-Mallart and M. Robert, *Chem. Soc. Rev.*, 2020, **49**, 5772–5809.
17 H. Takeda, C. Cometto, O. Ishitani and M. Robert, *ACS Catal.*, 2017, **7**, 70–88.
18 A. M. Appel, J. E. Bercaw, A. B. Bocarsly, H. Dobbek, D. L. DuBois, M. Dupuis, J. G. Ferry, E. Fujita, R. Hille, P. J. A. Kenis, C. A. Kerfeld, R. H. Morris, C. H. F. Peden, A. R. Portis, S. W. Ragsdale, T. B. Rauchfuss, J. N. H. Reek, L. C. Seefeldt, R. K. Thauer and G. L. Waldrop, *Chem. Rev.*, 2013, **113**, 6621–6658.
19 H. Dobbek, *Science*, 2001, **293**, 1281–1285.
20 H. Dobbek, L. Gremer, R. Kiefersauer, R. Huber and O. Meyer, *Proc. Natl. Acad. Sci. U.S.A.*, 2002, **99**, 15971–15976.
21 J.-H. Jeoung and H. Dobbek, *Science*, 2007, **318**, 1461–1464.
22 M. Beley, J.-P. Collin, R. Ruppert and J.-P. Sauvage, *J. Chem. Soc., Chem. Commun.*, 1984, 1315.
23 M. Hammouche, D. Lexa, M. Momenteau and J. M. Saveant, *J. Am. Chem. Soc.*, 1991, **113**, 8455–8466.
24 Z. Guo, F. Yu, Y. Yang, C.-F. Leung, S.-M. Ng, C.-C. Ko, C. Cometto, T.-C. Lau and M. Robert, *ChemSusChem*, 2017, **10**, 4009–4013.
25 H. Rao, C.-H. Lim, J. Bonin, G. M. Miyake and M. Robert, *J. Am. Chem. Soc.*, 2018, **140**, 17830–17834.
26 C.-Y. Zhu, Y.-Q. Zhang, R.-Z. Liao, W. Xia, J.-C. Hu, J. Wu, H. Liu and F. Wang, *Dalton Trans.*, 2018, **47**, 13142–13150.
27 K. Mochizuki, S. Manaka, I. Takeda and T. Kondo, *Inorg. Chem.*, 1996, **35**, 5132–5136.

28 Z. Guo, C. Cometto, L. Chen, B. Ma, H. Fan, T. Groizard, W.-L. Man, S.-M. Yiu, K.-C. Lau, M. Robert and T.-C. Lau, *Nat. Catal.*, 2019, **2**, 801–808.
29 J. Caballero-Jiménez, F. Habib, D. Ramírez-Rosales, R. Grande-Aztatzi, G. Merino, I. Korobkov, M. K. Singh, G. Rajaraman, Y. Reyes-Ortega and M. Murugesu, *Dalton Trans.*, 2015, **44**, 8649–8659.
30 F. Möller, K. Merz, C. Herrmann and U.-P. Apfel, *Dalton Trans.*, 2016, **45**, 904–907.
31 J.-M. Chen, W. Wei, X.-L. Feng and T.-B. Lu, *Chem.–Asian J.*, 2007, **2**, 710–719.
32 M. M. El-Hendawy, N. J. English and D. A. Mooney, *Inorg. Chem.*, 2012, **51**, 5282–5288.
33 T. Ouyang, H.-H. Huang, J.-W. Wang, D.-C. Zhong and T.-B. Lu, *Angew. Chem., Int. Ed.*, 2017, **56**, 738–743.
34 T. Ouyang, H.-J. Wang, H.-H. Huang, J.-W. Wang, S. Guo, W.-J. Liu, D.-C. Zhong and T.-B. Lu, *Angew. Chem., Int. Ed.*, 2018, **57**, 16480–16485.
35 J. Jökel, F. Nyßen, D. Siegmund and U.-P. Apfel, *Dalton Trans.*, 2021, **50**, 14602–14610.
36 F. Möller, K. Merz, C. Herrmann and U.-P. Apfel, *Dalton Trans.*, 2016, **45**, 904–907.
37 F. Möller, L. Castañeda-Losada, J. R. C. Junqueira, R. G. Miller, M. L. Reback, B. Mallick, M. van Gastel and U.-P. Apfel, *Dalton Trans.*, 2017, **46**, 5680–5688.
38 L. K. Weavers, I. Hua and M. R. Hoffmann, *Water Environ. Res.*, 1997, **69**, 1112–1119.
39 J.-M. Lehn and R. Ziessel, *Proc. Natl. Acad. Sci. U.S.A.*, 1982, **79**, 701–704.
40 Y. Tamaki, T. Morimoto, K. Koike and O. Ishitani, *Proc. Natl. Acad. Sci. U.S.A.*, 2012, **109**, 15673–15678.
41 P. Gerschel, K. Warm, E. R. Farquhar, U. Englert, M. L. Reback, D. Siegmund, K. Ray and U.-P. Apfel, *Dalton Trans.*, 2019, **48**, 5923–5932.
42 L. Iffland, D. Siegmund and U.-P. Apfel, *Z. Anorg. Allg. Chem.*, 2020, **646**, 1–9.
43 M. Obermeier, F. Beckmann, R. S. Schaer, O. S. Wenger and M. Schwalbe, *Front. Chem.*, 2021, **9**, 751716.
44 D. F. Evans, *J. Chem. Soc.*, 1959, 2003–2005.
45 R. S. Drago, *Physical Methods for Chemists*, Saunders College Pub., Ft. Worth, 1992.
46 G. L. Miessler, P. J. Fischer and D. A. Tarr, *Inorganic Chemistry*, Pearson, Boston, 2014, Fifth edition.
47 L. Banci, A. Bencini, C. Benelli, D. Gatteschi and C. Zanchini, in *Structures versus Special Properties*, Springer Berlin Heidelberg, Berlin, Heidelberg, 1982, vol. 52, pp. 37–86.
48 P. G. Alsabeh, A. Rosas-Hernández, E. Barsch, H. Junge, R. Ludwig and M. Beller, *Catal. Sci. Technol.*, 2016, **6**, 3623–3630.
49 F. Neese, *Wiley Interdiscip. Rev.: Comput. Mol. Sci.*, 2018, **8**, e1327.
50 V. N. Staroverov, G. E. Scuseria, J. Tao and J. P. Perdew, *J. Chem. Phys.*, 2003, **119**, 12129–12137.
51 F. Weigend, *Phys. Chem. Chem. Phys.*, 2006, **8**, 1057–1065.
52 E. van Lenthe, E. J. Baerends and J. G. Snijders, *J. Chem. Phys.*, 1993, **99**, 4597–4610.
53 E. van Lenthe, E. J. Baerends and J. G. Snijders, *J. Chem. Phys.*, 1994, **101**, 9783–9792.
54 C. van Wüllen, *J. Chem. Phys.*, 1998, **109**, 392–399.
55 B. I. Dunlap, J. W. D. Connolly and J. R. Sabin, *J. Chem. Phys.*, 1979, **71**, 3396–3402.
56 O. Vahtras, J. Almlöf and M. W. Feyereisen, *Chem. Phys. Lett.*, 1993, **213**, 514–518.
57 F. Neese, F. Wennmohs, A. Hansen and U. Becker, *Chem. Phys.*, 2009, **356**, 98–109.
58 R. Izsák and F. Neese, *J. Chem. Phys.*, 2011, **135**, 144105.
59 R. Izsák, F. Neese and W. Klopper, *J. Chem. Phys.*, 2013, **139**, 094111.
60 D. A. Pantazis, X.-Y. Chen, C. R. Landis and F. Neese, *J. Chem. Theory Comput.*, 2008, **4**, 908–919.
61 V. Barone and M. Cossi, *J. Phys. Chem. A*, 1998, **102**, 1995–2001.
62 M. Garcia-Ratés and F. Neese, *J. Comput. Chem.*, 2020, **41**, 922–939.